Nanoparticle Mediated Tumor Vascular Disruption: A Novel Strategy in Radiation Therapy

Nanoparticle Mediated Tumor Vascular Disruption:

A Novel Strategy in Radiation Therapy

Sijumon Kunjachan[1], Alexandre Detappe[1,2], Rajiv Kumar[1,3], Thomas Ireland[4], Lisa Cameron[5], Douglas E. Biancur[1], Vincent Motto-Ros[2], Lucie Sancey[2], Srinivas Sridhar[1,3], Mike Makrigiorgos[1], Ross I Berbeco[1*]*

1 - Department of Radiation Oncology, Brigham and Women's Hospital, Dana-Farber Cancer Institute and Harvard Medical School, Boston, MA, USA

2 - Institut lumière matière, Université Claude Bernard Lyon1-CNRS, Université de Lyon, France

3 - Nanomedicine Science and Technology Center and Department of Physics, Northeastern University, Boston, MA, USA

4 - LA-ICP-MS and ICP-ES Laboratories, Boston University, Boston, MA, USA

5 - Department of Pediatric Oncology, Dana-Farber Cancer Institute, Boston, MA, USA

ABSTRACT

More than 50% of all cancer patients receive radiation therapy. The clinical delivery of curative radiation dose is strictly restricted by the proximal healthy tissues. We propose a dual-targeting strategy using *vessel-targeted*-radiosensitizing gold nanoparticles and *conformal*-image guided radiation therapy to specifically amplify damage in the tumor neoendothelium. The resulting tumor vascular disruption substantially improved the therapeutic outcome and subsidized the radiation/ nanoparticle toxicity, extending its utility to intransigent or non-resectable tumors that barely respond to standard therapies.

KEYWORDS: *Gold Nanoparticles; Image-Guided Radiation Therapy; Endothelial Radiation Damage; Tumor Vascular Disruption*

Nanoparticles for radiation therapy have been an active area of research for several decades in oncology. More than 50% of cancer patients receive therapeutic radiation at some stage of their treatment course. Although highly effective for inflicting cellular damage, the specificity of radiation therapy is mainly derived from the geometric restriction of radiation beams. Sparing of healthy tissues and organs from radiation can be particularly challenging when treating tumors that are located in deep-seated anatomical locations. A strategy to intensify the tumor damage without adding additional risk to the healthy tissue is extremely advantageous in the clinic.

Multifunctional metallic nanoparticles have excellent potential as radiosensitizing agents primarily due to the superior interaction cross-section for high-*z*-elements when irradiated with low-energy x-rays[1]. This interaction results in the emission of short-range photoelectrons and Auger electrons which can impose damage to the tumor cellular or sub-cellular structures[2, 3]. Gold nanoparticles (AuNP) are of interest in radiation therapy due to its high k-edge (≈81 keV) and biocompatibility. In contrast to *i.v.* administered radioactive probes, gold is non-toxic in moderate quantities[4-6]. By specifically targeting AuNP to malignant tumor cells using 'enhanced permeability and retention' (EPR)- driven passive or peptide-/ antibody- mediated active tumor targeting, radiation damage can be invoked to the tumor cells upon irradiation[7-16]. Several preclinical studies have demonstrated this in different preclinical tumors, including prostate, breast, head and neck, cervical, sarcoma, glioblastoma, colorectal and melanoma[14, 17-25].

Previous studies have examined the potential for a classic clonogenic effect in cancer cells leading to improved radiotherapeutic efficacy. To this end, EPR-mediated passive targeting has been used to attain high AuNP deposition in the tumor cells. Although there are several benefits

attributed to passive tumor targeting, recent preclinical and clinical studies have shown that EPR-mediated passive tumor targeting was significantly less efficient (≈2-fold) in slow-growing animal pancreatic adenocarcinoma (PDAC) models *versus* fast-growing models[26-32]. This is primarily due to the fact that slow-growing tumors possess more mature and intact tumor blood vessels, amply sheathed by α-SMA and pericytes, leading to less vascular leakiness compared to the rapidly growing (aggressive) tumors which host leaky immature vessels[30, 33]. EPR is highly variable not only among different tumors, but also within the same tumor type, and often within different sub-regions of a single tumor[27, 28, 34].

Another critical factor that hampers drug/ nanoparticle delivery to the tumor cells is the highly heterogeneous and dense fibrotic microenvironment of solid tumor (especially in PDAC tumor). It is therefore extremely difficult for anticancer drugs (for ex. Gemcitabine), proteins, peptides or antibodies to diffuse and penetrate through the tumor interstitium to reach the cancer cells[29, 35]. In principle, this inherent tumor pathophysiology which regulates the poor diffusion of nanoparticles (beyond tumor vasculature and its periphery) is a serious limitation for cellular AuNP-mediated radiation therapy[35].

Tumor neovasculature is an important target for both chemo- and radiation- therapy[36-39]. Studies show that even clonogenic cellular dysfunction due to radiation is primarily mediated by the microvascular endothelial damage[36, 40-42]. To this end, chemical vascular disrupting agents have been shown to be effective either alone or in combination with radiation therapy. However, recent clinical trials showed severe off-target toxicity issues associated with chemical vascular disrupting agent therapies[41-44]. On the other hand, targeted-AuNP can minimize off-

target localization, and improve the overall localization at the tumor endothelium. In addition to this, the mm-scale accuracy of modern clinical image-guided radiation therapy can largely avoid AuNP activation in other healthy organs. This "two-fold targeting strategy" will minimize the normal tissue toxicity and consequently improve the therapeutic efficacy considerably[24, 45-47].

We have proposed a dual-targeting strategy by specific targeting of the tumor blood vasculature with targeted-gold nanoparticles and image-guided irradiation to improve radiation outcome by inducing vascular damage. Using Monte Carlo simulations, empirical electron range data and analytical calculations, our previous studies clearly show that gold nanoparticles will contribute to substantial dose enhancement to the tumor endothelial cells even without a specific cellular uptake[45]. In the following study, we experimentally validated the hypothesis that tumor-specific vascular disruption could be mediated by the administration of targeted gold nanoparticle followed by targeted irradiation in pancreatic tumor model. In our experimental design, gold nanoparticles were co-functionalized with a targeting- and imaging- ligand and injected into mice-bearing (Panc-1) pancreatic tumor xenografts (≈1.2 mg/g of Au i.v.). The tumor was then irradiated (10 Gy) and the vessel-damage response was assessed using a series of different analytical / imaging techniques *in vitro* and *in vivo*. The schematic depiction illustrates some of the prototypical responses of vessel rupture post-irradiation using gold nanoparticles, as further demonstrated in this study (Figure 1A-B).

PEGylated gold nanoparticles (AuNP) were prepared and co-functionalized with *Arg-Gly-Asp* (-RGD), a tumor neovascular targeting ligand and a near infrared dye, AF647. The bi-functional gold nanoparticle was prepared using a standard two-step process as described in the Materials

and Methods section. The THPC-stabilized nanoparticle were further functionalized to impart carboxylic (-COOH) and amino ($-NH_2$) pendant groups which further undergoes EDC coupling reaction to covalently attach -RGD and AF-647 moieties, the targeting and the imaging agents (Figure 2A). Besides the high k-edge, the relative ease of AuNP multi-functionalization, and its superior stability *vis-a-vis* for ex. micelles, liposomes, lipid nanoparticles, antibody-conjugates etc., extends its utility in radiation therapy. PEG-functionalization, by virtue of its higher hydrophilicity and stearic hindrance abilities, reduces the opsonization and improves the overall circulation kinetics and tumor accumulation. A near infrared dye-AF647 was chemically tagged to the AuNP to facilitate fluorescence/ confocal imaging. RGD (*Arg-Gly-Asp*), an oligopeptide, has high affinity for the transmembrane heterodimer $\alpha_v\beta_3$ integrin receptors which are highly over-expressed on the activated tumor neoendothelium. Since its inception in the 1980's, it has been used as a standard tumor vascular targeting ligand[28, 48, 49]. For the remainder of this study, the neovascular-targeted (-RGD), PEGylated and fluorophore-tagged AuNP formulation will be referred to as RGD:AuNP. With a spherical morphology, the core size of the RGD:AuNP was found to be ≈ 2-3 nm (by TEM imaging), and a hydrodynamic size of ≈ 8-10 nm was measured by DLS (Figure 2B-C). Size plays a determinant role in predicting the radiotherapeutic benefits. Several studies have demonstrated that AuNP with the size of ≈ 10-12 nm can produce a high radiosensitization effect[50]. The avg. zeta potential (surface charge) was -11.07 ± 1.07 in PBS (7.4). Absorption and fluorescence spectra of RGD:AuNP showed the integrity of AF-647 post-labeling by listing distinct peaks at the anticipated absorption/ fluorescence λ_{max} of 650/ 668 nm (Figure 2D).

For optimal therapeutic response, favorable *in vivo* accumulation and tumor blood vessel localization of nanoparticles in the tumor is crucial. To investigate the AuNP distribution profile in Panc-1- tumor bearing mice, we performed a series of high-resolution imaging techniques at early (1 h, post-*i.v.*) and late (24 h, post-*i.v.*) time points after RGD:AuNP administration. When STEM (Scanning transmission electron microscopy) imaging and TEM (Transmission electron microscopy) imaging assessed the early (1 h-*p.i.*) uptake kinetics of RGD-AuNP, LIBS (Laser-induced breakdown spectroscopy), fluorescence/ bright-field imaging and ICPMS (Inductively coupled plasma mass spectrometry) studies were used to trace the late localization (24 h-*p.i.*) of RGD-AuNP. Early distribution of AuNP in the tumor endothelium was detected as bright contrast signals in the STEM-EDX imaging (Figure 3A-B). Distinct Au peaks simultaneously corroborating with the bright signals (inset) were obtained using the EDX spectral read-outs. Furthermore, in a functional tumor blood vessel, large clusters of nanoparticles were actively taken up by the tumor endothelial cells as observed using TEM imaging (Figure 3C-E). In line with the previous reports, the uptake of RGD:AuNP may be primarily mediated by the active clathrin/caveolae- mediated endocytosis[51-54]. However, using non-targeted gold nanoparticles, no active endothelial uptake was observed (Figure S1). At 24 h post-*i.v.* injection, localization of RGD:AuNP was visualized close to the tumor blood vessels (Figure 3F-H). LIBS imaging, a novel advanced technique to specifically detect heavy metals/ elements showed heterogeneous distribution of gold (RGD:AuNP) in the tumor tissue[55, 56]. The spectral read-outs resonated with corresponding peaks for gold in the treated-samples *vs.* non-treated samples (Figure 3I-L). More to it, the (bio) distribution of RGD:AuNP in the tumor and other vital organs were measured with IC-PMS at 24 h-post-*i.v.*. Preferentially high accumulation in the tumor was apparently observed (Figure 3M). Other reported studies have shown that ≈10 nm-sized gold nanoparticles

that accumulate in the liver (kupffer cells) are eventually cleared by the hepato-biliary pathways[57]. In addition to this, the collimated radiation set-up that we employed largely reduces RGD:AuNP activation in off-target organs such as the liver. This has been confirmed by assessing the radiation dose distribution in tumor and other organs (which is explained in the upcoming sections). Due to the presence of over-expressed integrin receptors in the activated tumor endothelium of PDAC tumors, strong co-localization between RGD:AuNP and tumor blood vessels was observed *in vivo* at 24 h-*p.i.* using fluorescence imaging (Figure 3N).

In the following *in vitro* and *in vivo* results, the group receiving both RGD:AuNP and irradiation is referred to as +RGD:AuNP/+IR, the group receiving RGD:AuNP alone is referred to as +RGD:AuNP/–IR, the group receiving irradiation alone is referred to as –RGD:AuNP/+IR, and the group receiving neither AuNP nor irradiation is –RGD:AuNP/–IR. To validate the hypothesis of endothelial damage using RGD:AuNP upon irradiation, we performed an *in vitro* study using human umbilical vein endothelial cells (HUVEC) over-expressing the $\alpha_v\beta_3$ integrins during proliferation. By using a set of treated and non-treated controls (+RGD:AuNP/+IR, +RGD:AuNP/–IR, –RGD:AuNP/+IR and –RGD:AuNP/–IR), three different radiation doses (10 Gy, 5 Gy, and 0 Gy) were tested *in vitro*. Results obtained from the crystal violet assay displayed obvious qualitative differences between the treated (10 Gy, 5 Gy) and the non-treated (0 Gy) samples (Figure 4A). Unlike colony forming tumor cells, endothelial cells formed a single monolayer in the plates. The cells were therefore lysed to extract the stain from viable cells and the absorbance was measured at 590 nm. A statistically significant difference ($P<0.05$) in the HUVEC survival was observed for the +RGD:AuNP/+IR (10 Gy) sampled *vs.* the un-irradiated controls (58% *vs.* 98%) (Figure 4B). In addition, the sensitivity enhancement ratios

(SER, defined as the ratio of survival fractions after irradiation with and without nanoparticles) were calculated at 10 Gy and 5 Gy, and was found to be 1.2 ± .022 and 1.0 ± 0.028, respectively. Furthermore, on assessing the morphological changes in the HUVEC cells post-IR using phase contrast microscopy, increased endothelial cell rupture was observed for the radiation-treated ones (+RGD:AuNP/+IR) compared to non-treated samples (+RGD:AuNP/–IR and –RGD:AuNP/–IR) samples (Figure 4C), demonstrating the effect of the radiation. Nearly two-fold differences (33% *vs.* 41% *vs.* 95%) in the cell survival were observed between the RGD:AuNP treated/ irradiated group *vs.* non-treated group (Figure 4D). Furthermore, the uptake of nanoparticles (RGD-AuNP) was also compared with the respective survival in these *in vitro* endothelial models (see supplementary Figure S2).

Clinical radiation therapy of pancreatic cancer is often limited by the close proximity of organs-at-risk such as liver, duodenum, spleen and kidneys. In our study, we used a Small Animal Radiation Research Platform (SARRP) to perform image-guided radiation studies (Xtrahl, Inc.). By applying collimated radiation beams from two orthogonal angles, optimal tumor coverage was achieved and the exposure to other organs was grossly minimized (Figure 5A). To corroborate this, we performed image-guided dosimetry studies (Muriplan V.1.3.0) to determine the dose distribution in the tumor and normal tissues (Figure 5B). The results clearly indicate that >80% of the tumor region received a radiation dose of at least 10 Gy while the normal tissues were largely spared (<5%) (Figure 5C-D). Further histological staining of the adjacent muscle tissue showed no apparent radiation damage (see supplementary Figure S3). This set-up ensures maximum dose at the tumors with minimal effect on other healthy tissues / organs.

We further evaluated the potential of RGD:AuNP to induce tumor vascular damage in Panc-1 tumor xenografts at 24 h post-IR. 3D-confocal imaging was performed on excised tumor tissue pre-injected with a standard vessel marker, FITC-dextran (70 kDa; 60 µL of 1 mg/ml). For the +RGD:AuNP/+IR cohort, a high degree of specific vascular damage was observed compared to the respective controls (Figure 6A-D). The tumor endothelial cells were severely damaged by the +RGD:AuNP/+IR combined treatment. However in the respective controls, intact blood vessels with consistent endothelial integrity / functionality and uniformity were noticed (Figure 6B-D). Of note, two different types of vascular damage were apparently visible: fragmented vessels and diffused vessels (see supplementary Figure S4). Bright-field imaging was further employed to assess the morphological damage at the single vessel scale. Complete rupture of tumor vascular endothelium and damage to the vessel was clearly evident further confirming the previous results (Figure 6A). Partially segregated endothelial cells were present in the vicinity of damage site (cf. arrowheads). Essentially, the control batch showed normal tumor vascularity and endothelial integrity without any rupture (Figure 6F-H). We performed CD34 stainings to specifically detect the damage at the tumor microvasculature. To this end, large depletion of vessel structure and integrity was seen in the +RGD:AuNP/+IR samples compared to the respective controls (Figure 6I-L). At higher magnifications (2500x), TEM imaging clearly showed unambiguous damage to the tumor endothelium and the disruption of tumor blood vessel (Figure 6M). In the controls, however, endothelial cells were intact and sufficiently protected by the basement membrane (BM) and pericytes (Figure 6N-P). All of these observations using diverse techniques to evaluate different aspects of damage clearly show that

the targeted nanoparticles induced specific, catastrophic vascular damage in pancreatic tumors following irradiation.

In order to assess the direct radiation damage response at the molecular level, we measured overall tumor suppression and specific DNA damage (double-strand breaks) using H&E and γ-H2AX staining. Considerable reduction in the tumor proliferation and massive cell death was observed for the +RGD:AuNP/+IR samples compared to the respective controls (Figure 7A-D). Assuming the effect to be a more generic tumor suppression response, we further investigated the possibilities for specific radiation damage. The effect of irradiation on the tumor and tumor endothelial cells at the DNA level was measured by using γ-H2AX staining, taking into account recent experimental evidence of the temporal variations of γ-H2AX positive foci formation in tumor tissue post-IR[58]. We irradiated tumors +/- RGD:AuNP and dissected the tumors 30-40 minutes post-IR. γ-H2AX foci-formation in the tumor specimens showed a high degree of DNA double-strand breaks in the +RGD:AuNP/+IR samples (Figure 7E) compared to the controls (Figure 7F-H). Additionally, a large effect on the tumor endothelial cells was also observed (Figure 7I-J). Quantification of the DNA double strand breaks by γH2AX staining showed ≈ 3-fold increase ($P<0.001$) in the radiation specific DNA damage in the 'nanoparticle-radiation' group (+RGD:AuNP/+IR: 57%) compared to the 'radiation only' group (–RGD:AuNP/+IR: 19%), and almost ≈ 10-fold difference ($P<0.001$) compared to other controls (+RGD:AuNP/–IRR: 6% and –RGD:AuNP/–IR: 6%) (Figure 7K).

Our experimental findings support the original concept of targeted gold nanoparticles to induce specific tumor vascular damage during radiation therapy. Unlike cellular targeting,

which is often severely restricted by tissue (and physical) barriers, activated tumor endothelial targeting enables direct systemic access of nanoparticles to the over-expressed vascular targeting motifs. Moreover, shutting off a tumor blood capillary can affect numerous proliferating cancer cells, and an anti-tumorigenic (or anti-angiogenic) effect can be indirectly potentiated. By means of inducing both direct and indirect tumor cell killing mechanisms, we anticipate that this innovative treatment modality has promising clinical potential. Clinically administered chemical vascular disrupting agents have suffered from serious toxicity concerns. Combrestatin, a clinical vascular disrupting agent, showed fatal dose-limiting side effects including pulmonary embolism and coronary vasospasm when tested in human trials. In our approach, however, the activating radiation beams can be exclusively restricted to the tumor (containing actively-targeted gold nanoparticles). This dual-targeting platform could help maximize the therapeutic index by 1) increasing tumor damage and/or 2) reducing the amount of radiation dose needed to provide the same therapy effect and therefore limiting collateral damage to healthy tissues. The gold nanoparticles which are localized at other parts of the body (largely unaffected by radiation) will eventually be cleared by several phase degradation/ detoxification mechanisms[59]. The further impact of nanoparticle-mediated vascular damage using radiation therapy in terms of halting tumor blood vessel functionality and its downstream effects are currently under investigation. Therapy-induced hypoxia may be a challenge to a fractionated clinical approach, but this needs to be independently investigated. To summarize, this dual-targeting strategy holds great translational potential in radiation oncology. Application of this concept to other intransigent or non-resectable tumor types for which radiation delivery is limited by adjacent organs adds to the potential clinical impact. The data presented in this

paper represents the first in-depth experimental investigation of tumor vascular disruption with metallic nanoparticles, a novel strategy in radiation therapy.

ASSOCIATED CONTENT

Supporting Information

Materials and methods to characterize different polymeric nanomedicines are elaborated in the supplementary information's. This material is available free of charge via the Internet at http://pubs.acs.org.

AUTHOR INFORMATION

Corresponding Authors

*Tel.: +1-214-250-0923. Email: sijumon@gmail.com; skunjachan@lroc.harvard.edu
*Tel.: +1-617-525-7136. Email: rberbeco@lroc.harvard.edu

Notes

The authors declare no competing financial interest

ACKNOWLEDGMENTS

We acknowledge the efforts by Dr. Houari Korideck for assistance with the SARRP irradiations at Dana-Farber Cancer Institute, and the histology core facility at Brigham and Women's Hospital and Harvard Medical School, and the TEM imaging core facility at Harvard Medical School. This project was supported, in part, by a grant from the JCRT Foundation and by award numbers R03 CA164645 and R21 CA188833 from the National Cancer Institute (NCI). The

content of this manuscript is solely the responsibility of the authors and does not necessarily represent the official views of the NCI or NIH.

Figures

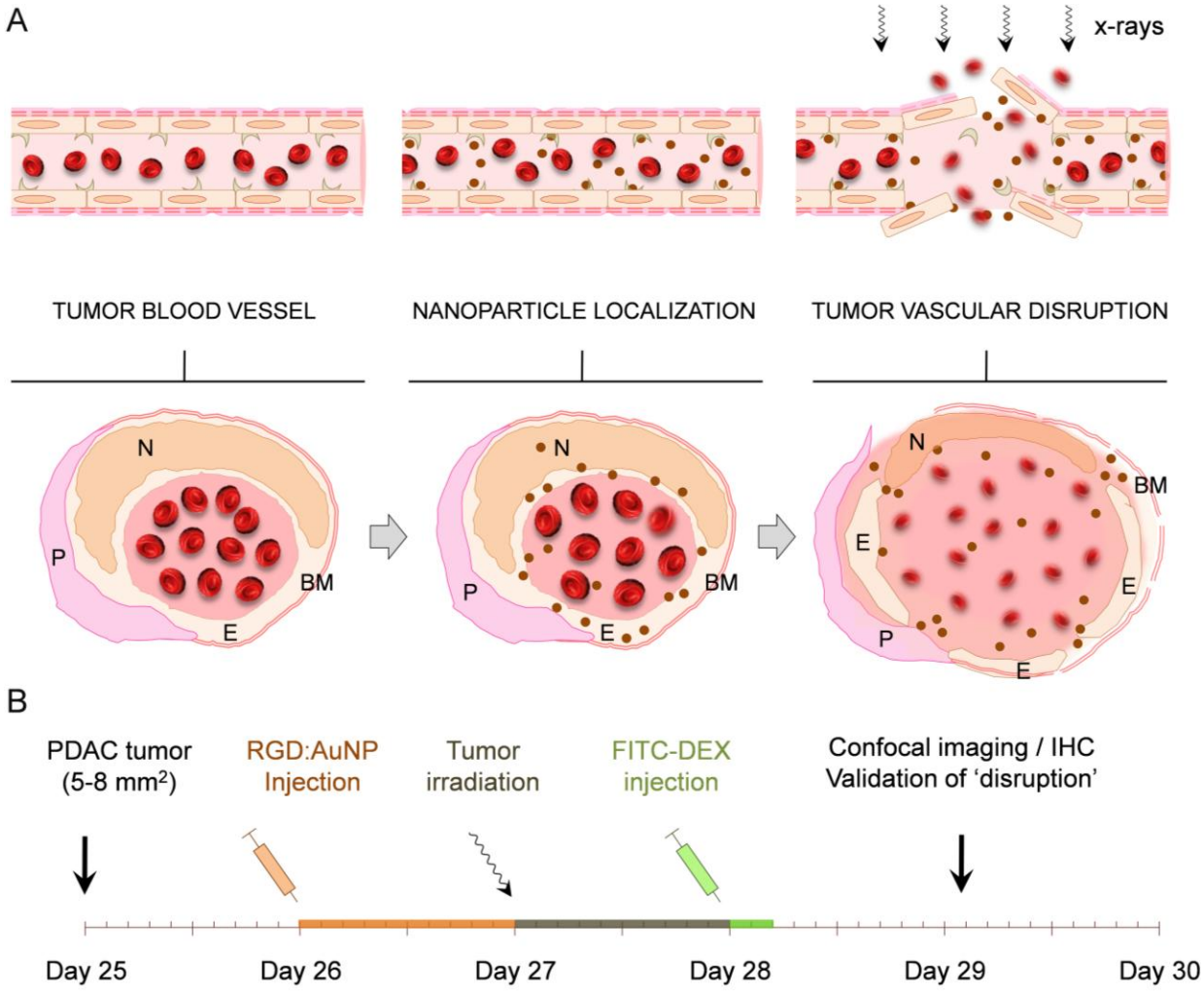

Figure 1. Experimental design and concept. (A) Schematic illustration of a tumor angiogenic blood vessel which, after active (vascular) targeting by gold nanoparticles to the $\alpha_v\beta_3$ integrin receptors and subsequent irradiation, suffers tumor endothelial disruption. The cross-sectional view depicts some of the prototypical responses related to 'vascular disruption' where the endothelium (E), pericytes (P), basement membrane (BM) and endothelial nuclei (N) undergo morphological changes and membrane destabilization leading to vessel rupture. (B) Roughly 25 days after s.c. tumor inoculation in NCr nude mice, ≈ 5-8 mm^2 sized Panc-1 tumor xenografts were obtained. The gold nanoparticles (referred to as RGD:AuNP) were synthesized and functionalized with the targeting ligand (*RGD*) and the imaging agent (AF-647). After proper characterization, RGD:AuNP (1.25 mg/ml equiv. Au in 200 µL) was administered into tumor-bearing mice and irradiated at 24 h post-*i.v.* injection. FITC-dextran (70 kDa; 1 mg/ml) was injected at 24 h after the irradiation and the mouse was sacrificed in 5-10 min to excise the tumor and other vital organs for further investigations.

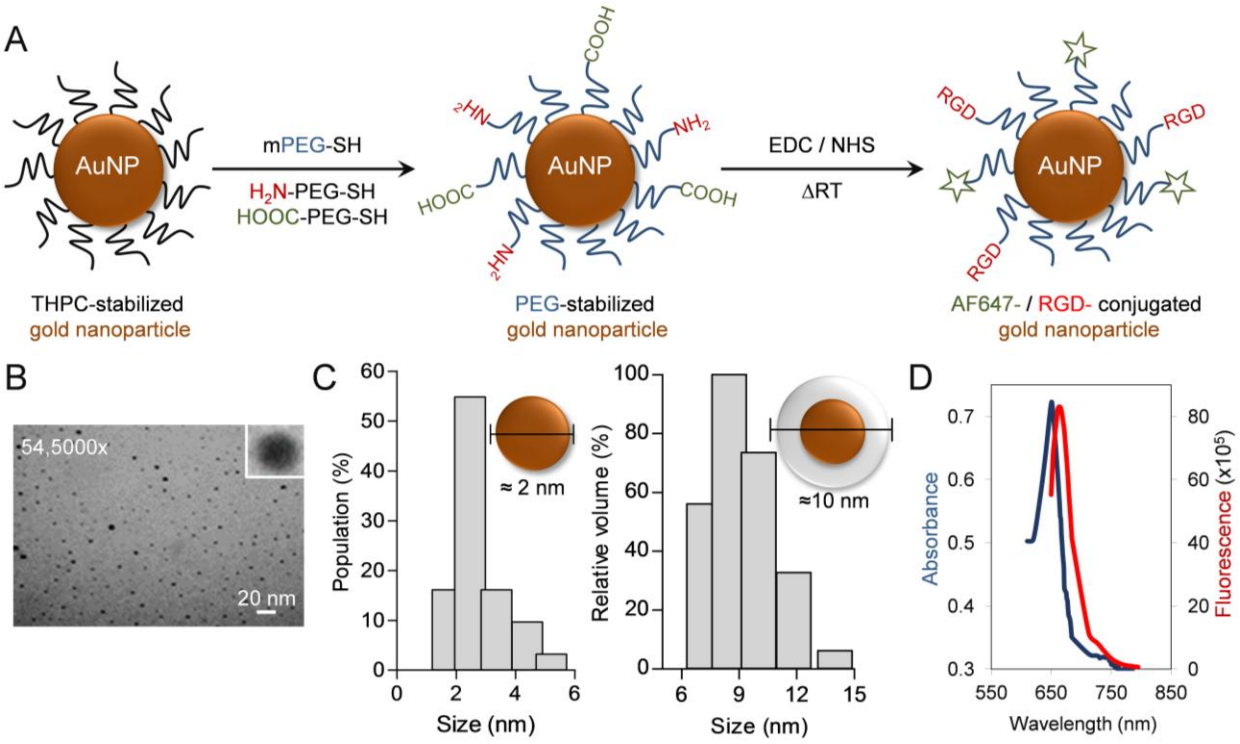

Figure 2. Chemical synthesis and characterization of functionalized gold nanoparticles for vascular tumor targeting. (A) Schematic representation of step-wise synthesis where PEGylated gold nanoparticles (AuNP) were bi-functionalized with *Arg-Gly-Asp* (RGD) and a near infrared imaging agent (AF647). The resultant product, PEG-RGD-AuNP-AF647 (or RGD:AuNP) was further purified and characterized. (B) RGD:AuNP showed spherical surface morphology (cf. inset) when analyzed using TEM imaging. (C) The particle size (core and hydrodynamic size) was measured by both TEM and DLS, and its core size was estimated to be ≈ 2-3 nm, whereas the hydrodynamic size was ≈ 8-10 nm. (D) The absorption and fluorescence spectra of RGD:AuNP was recorded post-labeling and it was found to be λ_{max} of 650/ 668 nm, in agreement with previous reported studies.

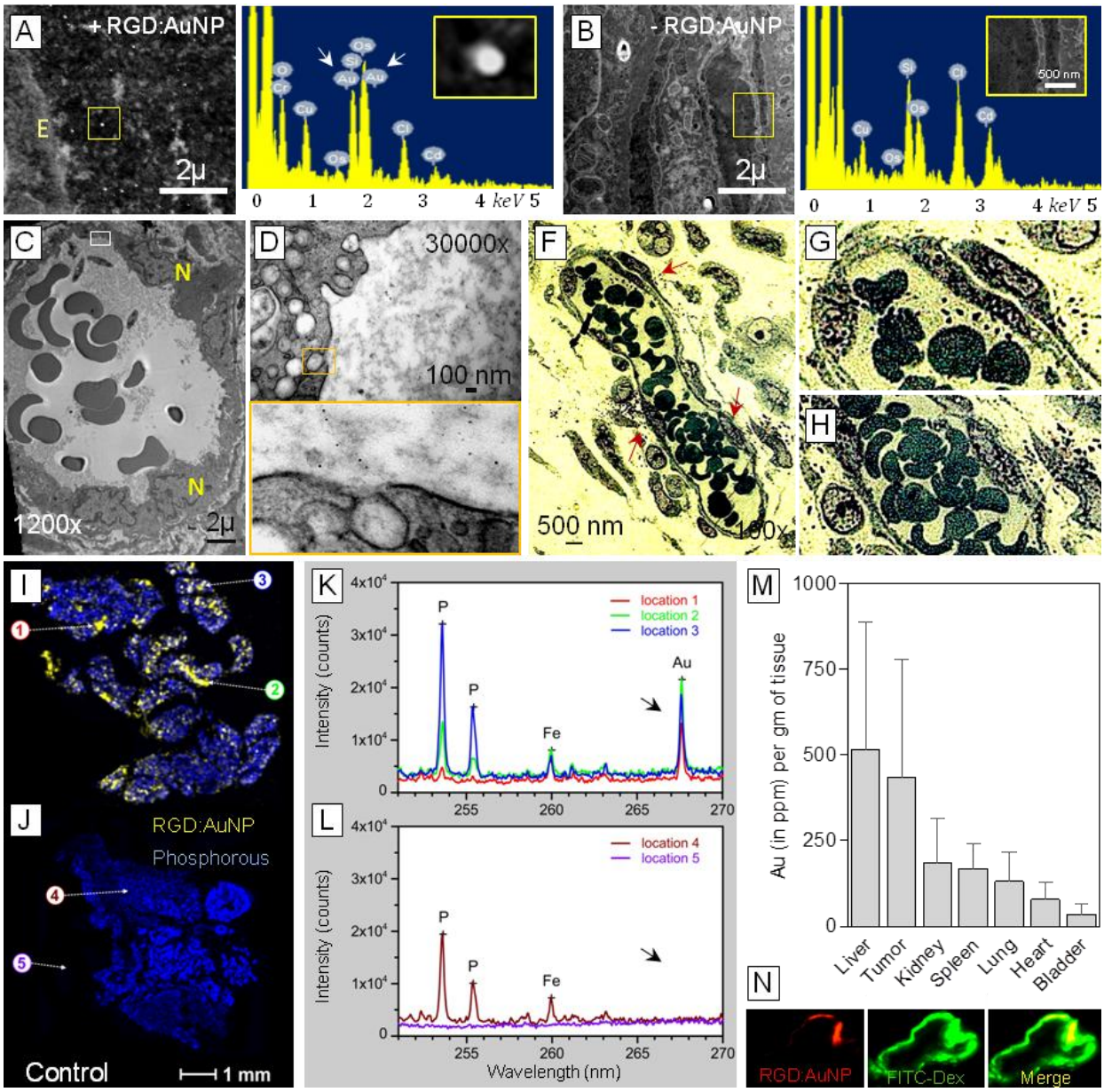

Figure 3. RGD:AuNP localization *in vivo* and tumor vascular targeting. (A-B) STEM (Scanning transmission electron microscopy) imaging detects the presence of targeted nanoparticles (indicated by bright contrast) on the tumor vessels at 1 h after RGD-AuNP injection in Panc-1 tumor bearing mice. The corresponding EDX spectral read-outs show distinct peaks which are specific for Au (see insets) in the samples. Apparently no gold was seen in the respective controls. (C-E) TEM images show the early uptake (1 h) of nanoparticles by the tumor endothelial cells *in vivo*. Higher magnified images (manual) indicate clathrin/ caveolae- mediated uptake at early/ late endosomal stages. E: Endothelium; N: Nucleus. (F-H) Bright field images show the RGD:AuNP localization close to the vessels at 1 h post-administration. Higher manual magnification of those images show the formation of AuNP aggregates close to the tumor endothelium. (I-L) Laser induced breakdown spectroscopy (LIBS) imaging was carried out to specifically confirm the presence of RGD:AuNP localization within the tumor 24 h post-*i.v.* Unlike TEM imaging, LIBS facilitates real-time monitoring of Au distribution within the tumors and directly correlates with the respective wavelengths in the corresponding spectral read-outs. (M) Biodistribution of RGD:AuNP in other organs was measured 24 h post-*i.v.* by ICPMS (n=3), and the

amount of Au was quantified based on the corresponding organ weight. The values represent average ± SD. (N) The co-localization of RGD:AuNP with FITC-dextran-labeled tumor endothelium was analyzed using fluorescence imaging. Strong co-localization is observed with (AF647-coupled) nanoparticle near the endothelial cells.

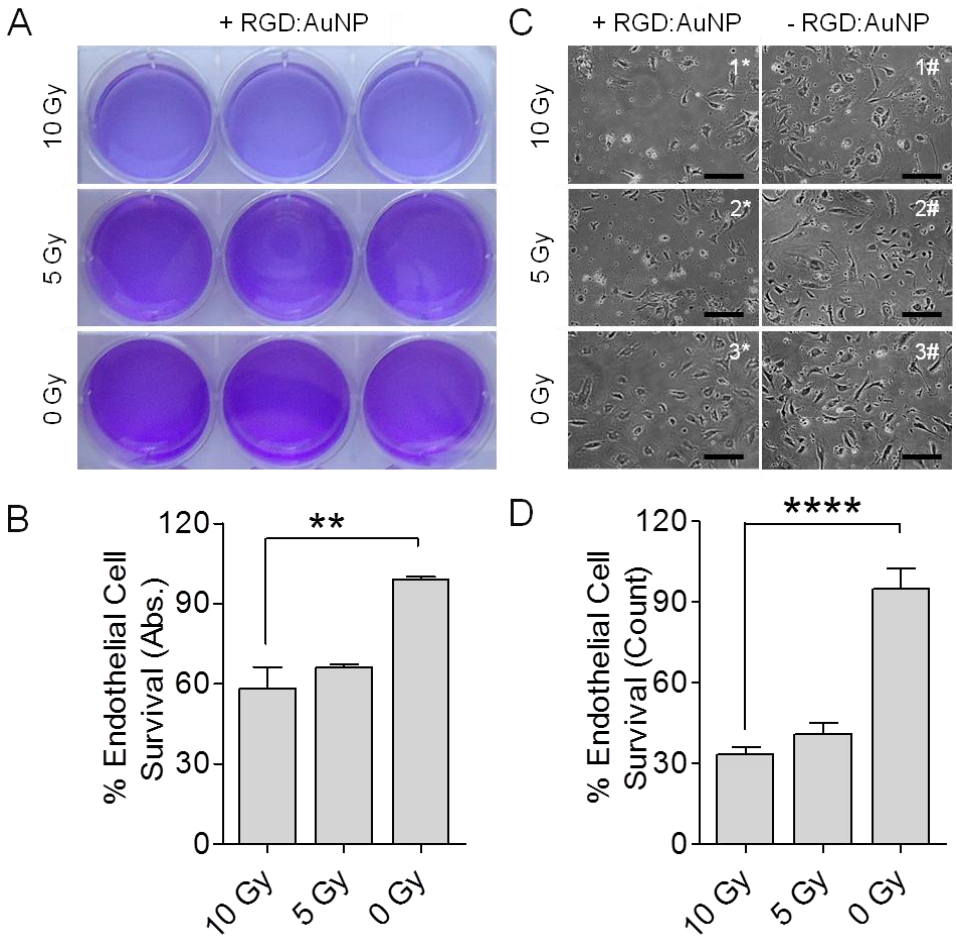

Figure 4. ***In vitro*** **radiation enhancement study.** Human umbilical vein endothelial cells were treated (+/–) RGD:AuNP (indicated by * and # respectively) and exposed to three different radiation doses: 0 Gy, 5 Gy and 10 Gy. All four treatment conditions were replicated in this study: +RGD:AuNP/+IR, +RGD:AuNP/–IR, –RGD:AuNP/+IR and –RGD:AuNP/–IR. (A-B) Crystal violet assay was performed on endothelial cells 1-week post-irradiation to detect the differences in the cell survival. The cells were lysed to extract and quantify crystal violet, by measuring its absorbance using a spectrophotometer at 590 nm. The values represent Mean ± SD, and all the data was normalized to its respective non-treated controls. ** $P < 0.05$. (C-D) Phase contrast microscopy was performed 1-week post-IR to visualize the proliferation (or survival) of the endothelial cells. Apparently, clear differences in the cell density was observed between the treated *vs.* non-treated group. Bar:10x. Further quantification of the phase contrast microscopic images was carried out by counting the viable cells/ frame (using ImageJ) in RGD:AuNP treated *vs.* non-treated in both irradiated and non-irradiated controls. In total, n=30 representative images/ condition were analyzed. The values represent Mean ± SD, and all the data was normalized to its respective non-treated controls. **** $P < 0.0005$.

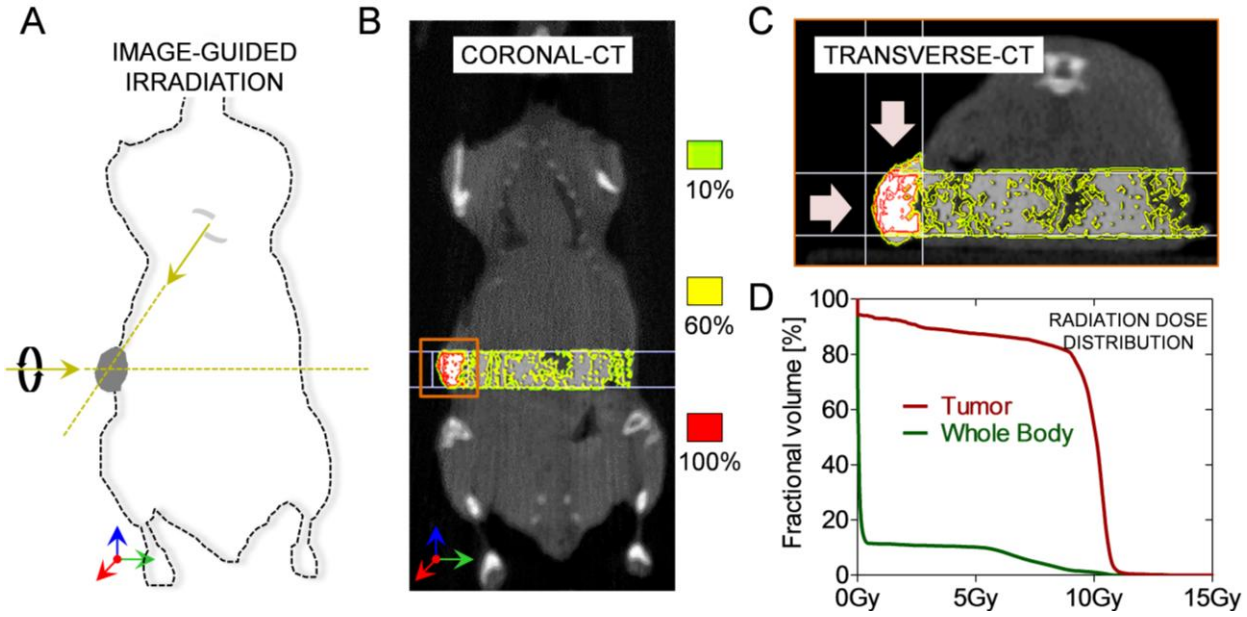

Figure 5. Small animal radiation research platform and radiation dose distribution *in vivo*. (A) Radiation set-up where each Panc-1 tumor xenograft was irradiated with 10 Gy (220 kVp) radiation beam. We used orthogonal, collimated beams in order to maximize the radiation dose exposure to the tumors and minimize the effect on (off-target) healthy tissues. (B) The representative coronal CT image shows the real-time distribution of radiation dose in the tumor and the surrounding tissue for RGD:AuNP-treated mouse with Panc-1 tumors. The isodose distribution shows high dose (95%-100%) in the tumor compared to the surrounding tissue. (C) Transverse (axial) section shows the isodose distribution specifically in the tumor. (D) The quantification of radiation doses from the cone beam CT images shows that more than 80% of the tumor received 10 Gy compared to the whole body.

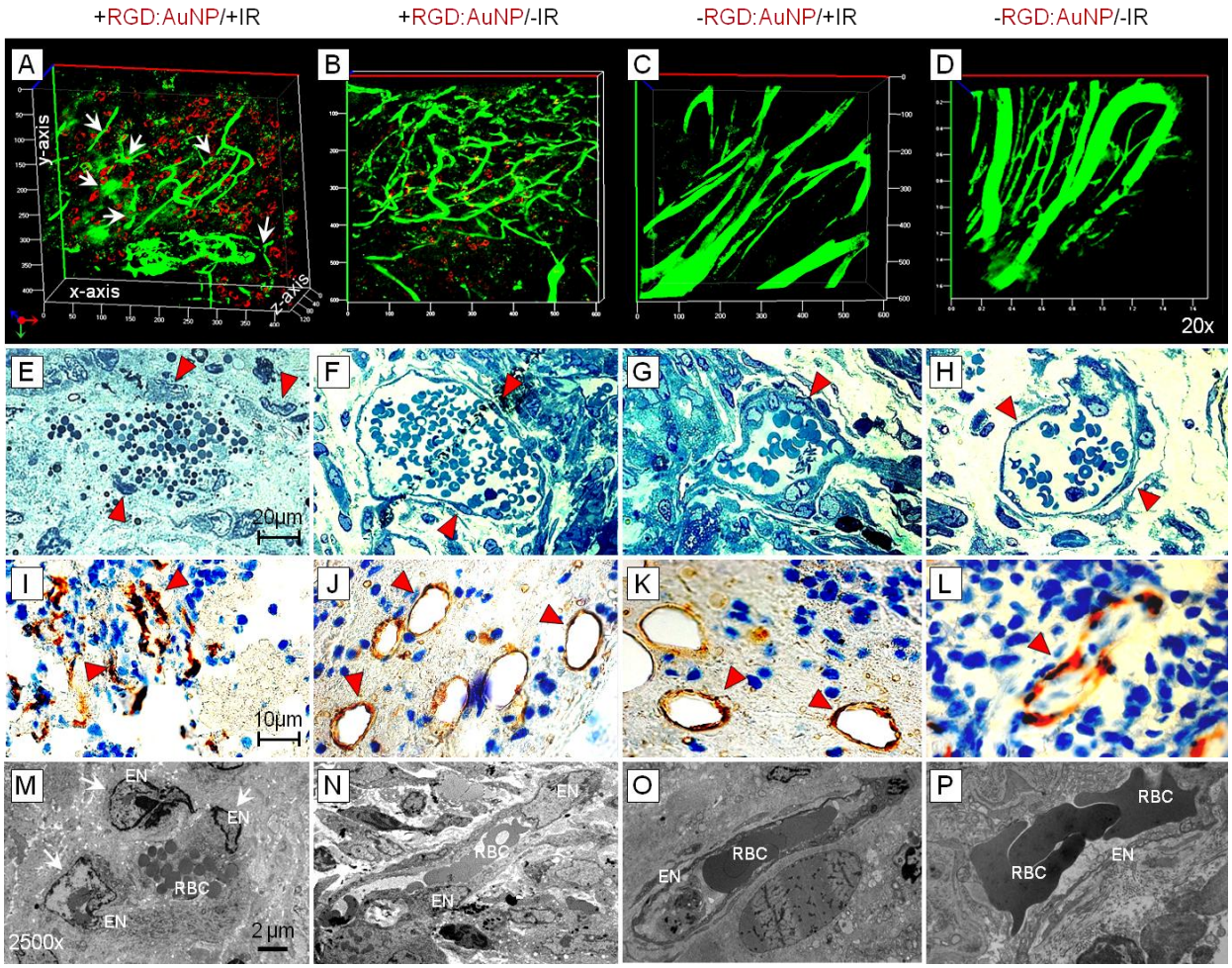

Figure 6. Imaging tumor vascular disruption. (A-D) Confocal imaging with RGD:AuNP (red) and FITC-Dextran (green) shows a high degree of vascular damage at the indicated locations (white arrows) and the presence of highly dense RGD:AuNPs in its close proximity, compared to the respective controls. (E-H) Bright field imaging shows damaged endothelial cells, and a change in the morphology of red blood cells clearly demonstrates loss of functionality for some of these vessels.. The control samples showed intact vessels and prominent endothelium. (I-L) CD34 IHC shows collapsed vessels and altered morphology (red marker) compared to the respective controls. (M-P) TEM imaging clearly confirms the endothelial rupture (see arrows). In the +RGD:AuNP/+IR samples, endothelial cells were detached and the cell nuclei damaged. The control samples showed high integrity and intact morphology. EN: Endothelial nucleus; RBC: Red blood cells; BM: Basement membrane.

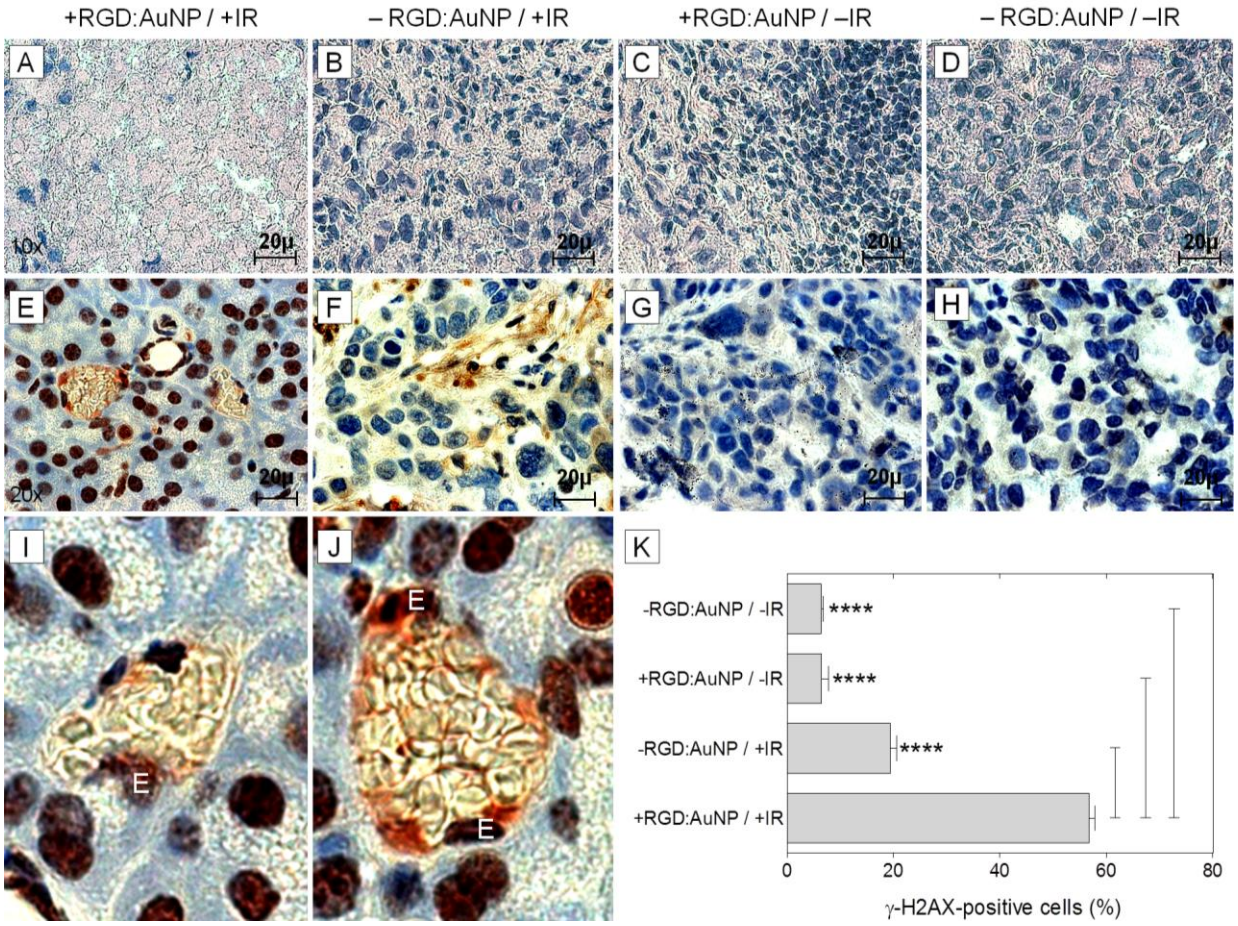

Figure 7. Assessing radiation outcome and specific DNA damage. (A-D) The H&E staining revealed the effect of radiation on the Panc-1 tumor xenograft. Massive cell death was observed in the RGD:AuNP treated samples compared to respective controls. (E-H) By γ-H2AX staining, we measured radiation induced DNA double strand breaks in the tumor. Color. Dark-brown: γ-H2AX-positive nuclei; Blue: Hematoxylin-positive nuclei (I-J) This effect was remarkable in the tumor blood vessels especially in the endothelial cell nucleus (denoted by 'E') showing high degree of radiation damage. (K) Quantification of the γ-H2AX signals showed significant increase (≈3-fold) in the magnitude of damage for the +RGD:AuNP/+IR samples compared to the controls (n= 60/cohort). The values represent average ± SD. **** $P < 0.0005$.

References

1. Hainfeld, J. F.; Dilmanian, F. A.; Slatkin, D. N.; Smilowitz, H. M. *J.Pharm.Pharmacol.* **2008,** 60, 977-985.
2. Jelveh, S.; Chithrani, D. B. *Cancers.(Basel)* **2011,** 3, 1081-1110.
3. Kumar, R.; Korideck, H.; Ngwa, W.; Berbeco, R. I.; Makrigiorgos, G. M.; Sridhar, S. *Transl.Cancer Res.* **2013,** 2.
4. Almeida, J. P.; Chen, A. L.; Foster, A.; Drezek, R. *Nanomedicine.(Lond)* **2011,** 6, 815-835.
5. Thakor, A. S.; Jokerst, J.; Zavaleta, C.; Massoud, T. F.; Gambhir, S. S. *Nano Lett* **2011,** 11, 4029-36.
6. Thakor, A. S.; Luong, R.; Paulmurugan, R.; Lin, F. I.; Kempen, P.; Zavaleta, C.; Chu, P.; Massoud, T. F.; Sinclair, R.; Gambhir, S. S. *Sci Transl Med* **2011,** 3, 79ra33.
7. Yang, Y. S.; Carney, R. P.; Stellacci, F.; Irvine, D. J. *ACS Nano.* **2014,** 8, 8992-9002.
8. Chithrani, D. B.; Dunne, M.; Stewart, J.; Allen, C.; Jaffray, D. A. *Nanomedicine.* **2010,** 6, 161-169.
9. Chithrani, B. D.; Ghazani, A. A.; Chan, W. C. *Nano Lett.* **2006,** 6, 662-668.
10. Berbeco, R. I.; Korideck, H.; Ngwa, W.; Kumar, R.; Patel, J.; Sridhar, S.; Johnson, S.; Price, B. D.; Kimmelman, A.; Makrigiorgos, G. M. *Radiat.Res* **2012,** 178, 604-608.
11. Jain, S.; Coulter, J. A.; Butterworth, K. T.; Hounsell, A. R.; McMahon, S. J.; Hyland, W. B.; Muir, M. F.; Dickson, G. R.; Prise, K. M.; Currell, F. J.; Hirst, D. G.; O'Sullivan, J. M. *Radiother.Oncol.* **2014,** 110, 342-347.
12. Hainfeld, J. F.; Smilowitz, H. M.; O'Connor, M. J.; Dilmanian, F. A.; Slatkin, D. N. *Nanomedicine (Lond)* **2013,** 8, 1601-1609.
13. Dorsey, J. F.; Sun, L.; Joh, D. Y.; Witztum, A.; Kao, G. D.; Alonso-Basanta, M.; Avery, S.; Hahn, S. M.; Al, Z. A.; Tsourkas, A. *Transl.Cancer Res* **2013,** 2, 280-291.
14. Joh, D. Y.; Sun, L.; Stangl, M.; Al, Z. A.; Murty, S.; Santoiemma, P. P.; Davis, J. J.; Baumann, B. C.; Alonso-Basanta, M.; Bhang, D.; Kao, G. D.; Tsourkas, A.; Dorsey, J. F. *PLoS.One.* **2013,** 8, 624-625.
15. Ngwa, W.; Kumar, R.; Sridhar, S.; Korideck, H.; Zygmanski, P.; Cormack, R. A.; Berbeco, R.; Makrigiorgos, G. M. *Nanomedicine (Lond)* **2014,** 9, 1063-1082.
16. Chen, W.; Ayala-Orozco, C.; Biswal, N. C.; Perez-Torres, C.; Bartels, M.; Bardhan, R.; Stinnet, G.; Liu, X. D.; Ji, B.; Deorukhkar, A.; Brown, L. V.; Guha, S.; Pautler, R. G.; Krishnan, S.; Halas, N. J.; Joshi, A. *Nanomedicine.(Lond)* **2014,** 9, 1209-1222.
17. Tree, A. C.; Ostler, P.; Hoskin, P.; Dankulchai, P.; Nariyangadu, P.; Hughes, R. J.; Wells, E.; Taylor, H.; Khoo, V. S.; van As, N. J. *Clin.Oncol.(R.Coll.Radiol.)* **2014,** 26, 757-761.
18. Atkinson, R. L.; Zhang, M.; Diagaradjane, P.; Peddibhotla, S.; Contreras, A.; Hilsenbeck, S. G.; Woodward, W. A.; Krishnan, S.; Chang, J. C.; Rosen, J. M. *Sci.Transl.Med.* **2010,** 2, 55ra79.
19. Lee, J.; Chatterjee, D. K.; Lee, M. H.; Krishnan, S. *Cancer Lett.* **2014,** 347, 46-53.
20. Masood, R.; Roy, I.; Zu, S.; Hochstim, C.; Yong, K. T.; Law, W. C.; Ding, H.; Sinha, U. K.; Prasad, P. N. *Integr.Biol.(Camb.)* **2012,** 4, 132-141.
21. Hainfeld, J. F.; Dilmanian, F. A.; Zhong, Z.; Slatkin, D. N.; Kalef-Ezra, J. A.; Smilowitz, H. M. *Phys Med Biol* **2010,** 55, 3045-59.

22. Zhang, X. D.; Chen, J.; Luo, Z.; Wu, D.; Shen, X.; Song, S. S.; Sun, Y. M.; Liu, P. X.; Zhao, J.; Huo, S.; Fan, S.; Fan, F.; Liang, X. J.; Xie, J. *Adv.Healthc.Mater.* **2014,** 3, 133-141.
23. Joh, D. Y.; Kao, G. D.; Murty, S.; Stangl, M.; Sun, L.; Al, Z. A.; Xu, X.; Hahn, S. M.; Tsourkas, A.; Dorsey, J. F. *Transl.Oncol.* **2013,** 6, 722-731.
24. Diagaradjane, P.; Shetty, A.; Wang, J. C.; Elliott, A. M.; Schwartz, J.; Shentu, S.; Park, H. C.; Deorukhkar, A.; Stafford, R. J.; Cho, S. H.; Tunnell, J. W.; Hazle, J. D.; Krishnan, S. *Nano.Lett.* **2008,** 8, 1492-1500.
25. Chang, M. Y.; Shiau, A. L.; Chen, Y. H.; Chang, C. J.; Chen, H. H.; Wu, C. L. *Cancer Sci.* **2008,** 99, 1479-1484.
26. Matsumura, Y.; Oda, T.; Maeda, H. *Gan To Kagaku Ryoho* **1987,** 14, 821-829.
27. Maeda, H.; Wu, J.; Sawa, T.; Matsumura, Y.; Hori, K. *J.Control Release* **2000,** 65, 271-284.
28. Kunjachan, S.; Pola, R.; Gremse, F.; Theek, B.; Ehling, J.; Moeckel, D.; Hermanns-Sachweh, B.; Pechar, M.; Ulbrich, K.; Hennink, W. E.; Storm, G.; Lederle, W.; Kiessling, F.; Lammers, T. *Nano.Lett.* **2014,** 14, 972-981.
29. Cabral, H.; Matsumoto, Y.; Mizuno, K.; Chen, Q.; Murakami, M.; Kimura, M.; Terada, Y.; Kano, M. R.; Miyazono, K.; Uesaka, M.; Nishiyama, N.; Kataoka, K. *Nat.Nanotechnol.* **2011,** 6, 815-823.
30. Harrington, K. J.; Mohammadtaghi, S.; Uster, P. S.; Glass, D.; Peters, A. M.; Vile, R. G.; Stewart, J. S. *Clin.Cancer Res.* **2001,** 7, 243-254.
31. Kunjachan, S.; Ehling, J.; Storm, G.; Kiessling, F.; Lammers, T. *Chem Rev* **2015**.
32. Kunjachan, S.; Jayapaul, J.; Mertens, M. E.; Storm, G.; Kiessling, F.; Lammers, T. *Curr.Pharm Biotechnol* **2012,** 13, 609-622.
33. Siegel, R. L.; Miller, K. D.; Jemal, A. *CA Cancer J.Clin.* **2015,** 65, 5-29.
34. Maeda, H.; Matsumura, Y. *Adv.Drug Deliv.Rev.* **2011,** 63, 129-130.
35. Hauert, S.; Berman, S.; Nagpal, R.; Bhatia, S. N. *Nano Today* **2013,** 8, 566-576.
36. Garcia-Barros, M.; Paris, F.; Cordon-Cardo, C.; Lyden, D.; Rafii, S.; Haimovitz-Friedman, A.; Fuks, Z.; Kolesnick, R. *Science* **2003,** 300, 1155-1159.
37. Arap, W.; Pasqualini, R.; Ruoslahti, E. *Science* **1998,** 279, 377-380.
38. Cooney, M. M.; van, H. W.; Bhakta, S.; Ortiz, J.; Remick, S. C. *Nat.Clin.Pract.Oncol.* **2006,** 3, 682-692.
39. Banerjee, D.; Harfouche, R.; Sengupta, S. *Vasc Cell* **2011,** 3, 3.
40. Potten, C. S. *Int J Radiat.Biol.* **1990,** 58, 925-973.
41. Siemann, D. W.; Rojiani, A. M. *Int.J.Radiat.Oncol.Biol.Phys.* **2005,** 62, 846-853.
42. Siemann, D. W.; Horsman, M. R. *Cell Tissue Res.* **2009,** 335, 241-248.
43. Mauceri, H. J.; Hanna, N. N.; Wayne, J. D.; Hallahan, D. E.; Hellman, S.; Weichselbaum, R. R. *Cancer Res.* **1996,** 56, 4311-4314.
44. Hinnen, P.; Eskens, F. A. *Br.J.Cancer* **2007,** 96, 1159-1165.
45. Berbeco, R. I.; Ngwa, W.; Makrigiorgos, G. M. *Int.J.Radiat.Oncol.Biol.Phys.* **2011,** 81, 270-276.
46. Berbeco, R. I.; Korideck, H.; Ngwa, W.; Kumar, R.; Patel, J.; Sridhar, S.; Johnson, S.; Price, B. D.; Kimmelman, A.; Makrigiorgos, G. M. *Radiat.Res.* **2012,** 178, 604-608.
47. Rahman, W. N.; Bishara, N.; Ackerly, T.; He, C. F.; Jackson, P.; Wong, C.; Davidson, R.; Geso, M. *Nanomedicine.* **2009,** 5, 136-142.
48. Ruoslahti, E.; Pierschbacher, M. D. *Science* **1987,** 238, 491-497.

49. Ruoslahti, E. *Matrix Biol* **2003,** 22, 459-65.
50. Zhang, X. D.; Wu, D.; Shen, X.; Chen, J.; Sun, Y. M.; Liu, P. X.; Liang, X. J. *Biomaterials* **2012,** 33, 6408-6419.
51. Chithrani, B. D.; Chan, W. C. *Nano.Lett.* **2007,** 7, 1542-1550.
52. Jiang, W.; Kim, B. Y.; Rutka, J. T.; Chan, W. C. *Nat.Nanotechnol.* **2008,** 3, 145-150.
53. Chithrani, B. D.; Stewart, J.; Allen, C.; Jaffray, D. A. *Nanomedicine.* **2009,** 5, 118-127.
54. Yang, C.; Uertz, J.; Yohan, D.; Chithrani, B. D. *Nanoscale.* **2014,** 6, 12026-12033.
55. Sancey, L.; Motto-Ros, V.; Busser, B.; Kotb, S.; Benoit, J. M.; Piednoir, A.; Lux, F.; Tillement, O.; Panczer, G.; Yu, J. *Sci Rep* **2014,** 4, 6065.
56. Sancey, L.; Kotb, S.; Truillet, C.; Appaix, F.; Marais, A.; Thomas, E.; van der Sanden, B.; Klein, J. P.; Laurent, B.; Cottier, M.; Antoine, R.; Dugourd, P.; Panczer, G.; Lux, F.; Perriat, P.; Motto-Ros, V.; Tillement, O. *ACS Nano.* **2015,** 9, 2477-2488.
57. Hirn, S.; Semmler-Behnke, M.; Schleh, C.; Wenk, A.; Lipka, J.; Schaffler, M.; Takenaka, S.; Moller, W.; Schmid, G.; Simon, U.; Kreyling, W. G. *Eur.J.Pharm.Biopharm.* **2011,** 77, 407-416.
58. Herter-Sprie, G. S.; Korideck, H.; Christensen, C. L.; Herter, J. M.; Rhee, K.; Berbeco, R. I.; Bennett, D. G.; Akbay, E. A.; Kozono, D.; Mak, R. H.; Mike, M. G.; Kimmelman, A. C.; Wong, K. K. *Nat.Commun.* **2014,** 5, 5870.
59. Kolosnjaj-Tabi, J.; Javed, Y.; Lartigue, L.; Volatron, J.; Elgrabli, D.; Marangon, I.; Pugliese, G.; Caron, B.; Figuerola, A.; Luciani, N.; Pellegrino, T.; Alloyeau, D.; Gazeau, F. *ACS Nano* **2015**.

GRAPHICAL ABSTRACT